Science Discovery Environment
2026, Vol. 1, No. 4, pp. 215–233
https://doi.org/10.11648/j.sdenv.20260104.14

Research Article

Spatiotemporal Analysis of Temperature Extremes Under Future Climate Scenarios in the Borana Zone, Ethiopia

Mikiyas Gebre Arrefaine[1, *], Tesfay Mekonnen Weldegerima[2]

[1]Ethiopian Meteorology Institute, West Oromia Meteorological Research Center, Jimma, Ethiopia
[2]Meteorology and Hydrology Faculty, Arba Minch University, Arba Minch, Ethiopia

Abstract

Climate change has intensified temperature extremes worldwide, with particularly severe implications for semi-arid regions such as southern Ethiopia. This study assessed historical and future temperature extremes across the Borana Zone using ENACTS observational datasets (1985–2014) and bias-corrected outputs from nine CMIP6 global climate models under SSP2-4.5 and SSP5-8.5 scenarios. Extreme temperature indices recommended by the Expert Team on Climate Change Detection and Indices (ETCCDI) were computed using the Climate Data Tool. Model performance was evaluated using correlation coefficient, mean error, mean absolute error, root mean square error, and index of agreement. Long-term trends were assessed using the Mann–Kendall test and Sen's slope estimator, while Pearson correlation analysis was employed to investigate relationships between temperature extremes and major large-scale climate indices, including ENSO, PDO, IOD, SOI, and AMO. Results indicate statistically significant increases in warm temperature indices (TN90p, TX90p, TNx, TXx) and significant decreases in cold extremes (TN10p and CSDI), indicating an overall warming climate with stronger nighttime warming. Future projections show substantial increases in mean temperature and warm spell duration under both emission scenarios, with the highest warming projected under SSP5-8.5 by the late twenty-first century. Diurnal temperature range is projected to decrease, reflecting accelerated increases in minimum temperature relative to maximum temperature. Significant relationships between several temperature extremes and large-scale climate indices demonstrate the influence of global climate variability on regional temperature behavior. These findings provide important scientific evidence for climate adaptation planning, drought preparedness, and sustainable management of pastoral systems in the Borana Zone.

Keywords

Borana Zone, CMIP6, Mann Kendall, Large Scale Climate Indices, Sen.'s Slope, Temperature Extremes

1. Introduction

According to recent IPCC data, the average global temperature increased by 0.85 ℃ between 1880 and 2012 [6]. The increase in the global average temperature, commonly referred to as global warming, has a substantial influence on many developing countries, particularly those in Sub-Saharan Africa. Because Ethiopia's economy depends on climate-sensitive industries like agriculture and pastoral systems, the repercussions of a changing climate are felt broadly

*Correspondence: Mikiyas Gebre Arrefaine (mikiyasgebre35@gmail.com)

Received: 4 October 2026; **Accepted:** 21 October 2026; **Published:** 6 November 2026

Copyright: © The Author(s), 2026. Published by Science Publishing Group. This is an **Open Access** article, distributed under the terms of the Creative Commons Attribution 4.0 License (http://creativecommons.org/licenses/by/4.0/), which permits unrestricted use, distribution and reproduction in any medium, provided the original work is properly cited.

in these nations [29].

One of Africa's largest nations, Ethiopia, is characterized by a complex physiography that includes the Dega (2,300-3,300 meters), Wionadega (1,500-2,300 meters), Kolla (500-1,500 meters), and Bereha (less than 500 meters) ranges, according to the Ethiopian Institute of Agricultural Research (EIAR, 2011). The country's complex geography is not the only factor influencing its climate; the Intertropical Convergence Zone (ITCZ), where the northeast and southeast trade winds meet as the Sun passes overhead, also plays a role [28, 49]. As a result, the ITCZ's seasonal migration causes distinct dry and rainy weather seasons.

The temporal and spatial variations in the climatic system (temperature), which are governed by these factors, may have an impact on a wide range of socioeconomic systems, such as livestock and agricultural systems, among others. Drought and other harsh weather conditions also affect populations of agropastoralists and lowland pastoralists. If future climatic extremes render traditional coping mechanisms inadequate, disaster managers will have to develop new management strategies. Emergency response plans, and economic disaster preparation that relies on historical weaknesses might no longer work [27, 55, 56].

According to future forecasts, countries and systems that currently have low levels of risk preparation will be extremely susceptible. The Greater Horn of Africa region is not new to the linkages between extreme weather and the spread and intensification of disasters, plagues, and conflicts. For example, the drought in 1984 exacerbated the Darfur war by causing food instability and starvation [60]. The earth's climate has fluctuated periodically due to a variety of natural and man-made factors [37, 41].

This study aimed to visualize the potential spatiotemporal features of extreme temperature events in the past and future. It also examined the relationship between large-scale climate indices and temperature extreme indices across the Study Area using data from the CMIP6 Climate Models, ETCCDI core indices, and the websites of large-scale climate indices. The ETCCDI Climate Indices can be used to measure and quantify climate variability and associated trends.

This study compared temperature patterns between ENACTS (1985-2014) and ESGF CMIP6 GCM Historical, Future (ssp2.45&ssp5.85) data in the semi-arid Borana zone in southern Ethiopia. Large-scale climate indices have a major impact on regional and global climate variability in addition to localized weather patterns [25]. Despite being far from their source, these indices reflect the main patterns of oceanic and atmospheric circulation that function on interannual to decadal timeframes and can teleconnection with regional climate, including temperature extremes [57]. Comprehending their impact is essential for understanding and forecasting climatic anomalies in East Africa and other regions of the world. Temperature anomaly extremes were correlated with large-scale climatic indices (AMO, El-Nino3.4, SOI, IOD and PDO) using Pearson Correlation.

2. Materials and Methods

2.1. Descriptions of the Study Area

The study is conducted in Borana, which is one of the Oromia Region's zones located in southern Ethiopia. Geographically, it is located between 3°00′ and 7°00′ north latitude and 37°00′ and 41°00′ east longitude, encompassing approximately 98848.8 km^2, as seen in Figure 1. Borana Zone has a diverse topography that ranges from 343 to 2452 meters above sea level. The Borana rangelands span around 1.9 million hectares. The region has a semi-arid savannah landscape, typified by gently sloping lowlands and floodplains planted primarily with grass and shrub [61].

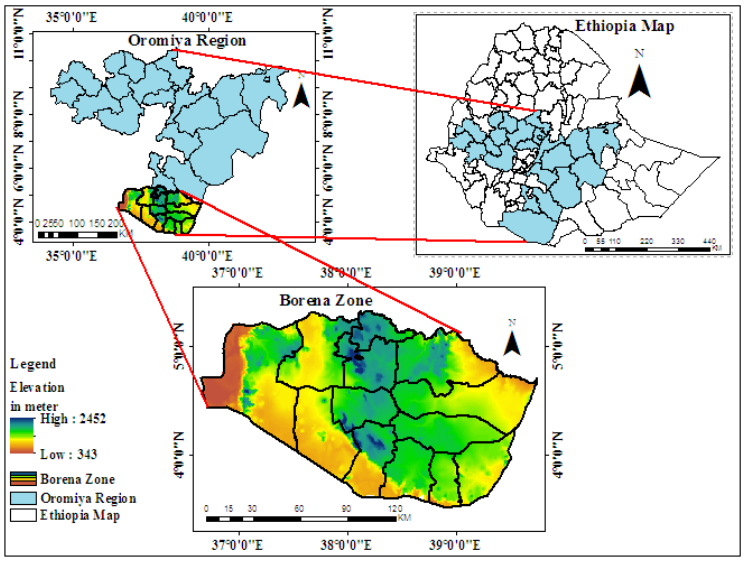


Figure 1. *Map of the Study area with elevation.*

2.2. Economic Conditions and Climates of the Study Area

Borana Zone has an average annual rainfall of 350 mm to roughly 900 mm, which is distributed over two rainy seasons: March to May and September to October. The area has a semi-arid to arid environment and is home to pastoral and agro-pastoral people. These communities rely only on climate-sensitive sectors (livestock raising and small-scale farming methods) for their survival. Farming is a relatively new activity in the area, promoted by the government to diversify methods of producing additional revenue for the family, and it is no longer done in some districts due to a lack of rainfall.

The Borana Zone has four climate types: hot dry, hot semi-arid, tropical wet or rainy, and mild temperate. In steppe-covered areas, the hot semi-arid climate predominates. In this climate zone, the average annual temperature ranges from 18 ℃ to 27 ℃, while the mean annual rainfall ranges from 410 to 820 mm. This is the climate in Borana's west and south [16]. The study location likewise has a tropical wet climate. In a tropical wet environment, the average temperature in the cold months is around 18 ℃, with an average annual rainfall of 680-2000 mm.

2.3. Data Collection

From Ethiopia Meteorological Institute, gridded daily Tmax, and Tmin data (ENACTS) for the research region from 1985 to 2014 were collected. Since, ENACTS data provides several benefits, including completeness and accessibility [18]. These data were used to evaluate the CMIP6 models (Table 1) in the current study. On the other hand, CMIP6 datasets for sea surface temperatures from nine climate models participating in CMIP6 were obtained from an Earth System Grid Federation website (https://esgf-node.llnl.gov/projects/cmip6) [13]. These data were utilized for future prediction of climate extreme indices. The CMIP6 models were selected depend on their high resolution and Availability of data which is useful for the climate indices study and also depending on the research conducted on the Performance evaluation and ranking of CMIP6 global climate models research by [38].

Furthermore, Climatic indicators include the Pacific Decadal Oscillation (PDO), Southern Oscillation Index (SOI), Indian Ocean Dipole (IOD), and Atlantic Multi-decadal Oscillation (AMO), with El-Nino3.4 being utilized in this study. The SOI, acquired from http://www.bom.gov.au/climate/current/soihtm1.shtml, depicts the measured surface air pressure differential between western (Tahiti) and eastern tropical Pacific (Darwin, Australia) during El Niño and La Niña events. Ethiopian researchers used these data [19, 50]. Download the Pacific Decadal Oscillation (PDO) data from https://www.ncdc.noaa.gov/teleconnections/pdo/data. The PDO is a long-term pattern of Pacific climate variability similar to El Niño. El-Nino3.4 the data were taken from the website (https://www.esrl.noaa.gov/). This data was used by Ethiopian researcher [36], who used it to connect large-scale climatic indices with local drought indices. [15] found that El Niño disrupts Ethiopia's Kiremt rainfall throughout the boreal summer season.

Table 1 shows the models that were selected depend on their high resolution and Availability of data which is useful for the climate indices study and also depending on the research conducted on the Performance evaluation and ranking of CMIP6 global climate models research by [38].

These Models are used by Ethiopian Researchers by [3, 11, 14, 22] for evaluation of General Circulation Models CMIP6 Performance and Future Climate Change.

Table 1. *Overview of CMIP6 models applied in this investigation.*

No.	CMIP6 model name	Country	Atmospheric Resolution (lon×lat in deg.)	Variant label
1	CMCC-ESM2	Italy	1.3 °×0.9 °	r1i1p1f1
2	CNRM-ESM2-1	France	1.4 °×1.4 °	r1i1p1f1
3	INM-CM4-8	Russia	2 °×1.5 °	r1i1p1f1
4	INM-CM5-0	Russia	2 °×1.5 °	r1i1p1f1
5	MIROC6	Japan	1.4 °×1.4 °	r1i1p1f1
6	MIROC-ES2L	Japan	2.8 °×2.8 °	r1i1p1f1
7	MPI-ESM1-2-HR	Germany	0.9 °×0.9 °	r1i1p1f1
8	MRI-ESM2-0	Japan	1.1 °×1.1 °	r1i1p1f1
9	NorESM2-MM	Norway	0.9 °×1.3 °	r1i1p1f1

2.4. Bias Correction for CMIP6 Data

The magnitude of climate change's influence is also determined by the principles of bias correction approaches [44]. As a result, the Climate Data Bias Corrector (CDBC) tool is used to correct the bias in historical and future climatic projections for three key climatic variables: rainfall, temperature (maximum and minimum), and solar radiation. [17] adopt the Quantile mapping approach for bias correction, which is known for its efficiency and low computing cost.

The GCM output was corrected using daily-observed air temperature, for reducing climatic bias

The correlation coefficient is given by Equation (1);

$$r = \frac{\frac{1}{2}\sum_{t=1}^{N}(X_t-\bar{X})(Y_t-\bar{Y})}{\sqrt{\frac{1}{2}\{\sum_{t=1}^{N}(X_t-\bar{X})^2\}\{\sum_{t=1}^{N}(Y_t-\bar{Y})^2\}}} \quad (1)$$

In Equation (1), $X_t$and Y_t are ENACT observational temperature data and CMIP6 Models Temperature data at time t, and $\overline{X}$ and $\overline{Y}$ arithmetic means of X_t and Y_t at time t respectively. N is the record length.

2.5. Determination of Climate Indices

In the current study, Climate data tool (CDT) was used for the computations of b temperature extremes. The temperature computed in present study were summarized in the Table 2.

Table 2. *List of the Climate Indices used in this Study are the following.*

ID (unit)	Indicator name	Definitions
SU25 (days)	Summer days	Annual count when TX (daily maximum)[25 ℃]
TXx (℃)	Hottest days	Monthly maximum value of daily maximum temp
TNx (℃)	Warmest nights	Monthly maximum value of daily minimum temp
TXn (℃)	Coldest days	Monthly minimum value of daily maximum temp
TNn (℃)	Coldest nights	Monthly minimum value of daily minimum Temp
TN10p (% days)	Cool nights	Percentage of days when TN\10th Percentile
TX10p (% days)	Cool days	Percentage of days when TX\10th Percentile
TN90p (% days)	Warm nights	Percentage of days when TN[90th Percentile
TX90p (% days)	Warm days	Percentage of days when TX[90th Percentile
WSDI (days)	Warm spell duration indicator	Annual count of days with at least 6 consecutive days when TX[90th Percentile
CSDI (days)	Cold spell duration indicator	Annual count of days with at least 6 consecutive days when TN\10th Percentile
DTR (℃)	Diurnal temperature range	Monthly mean difference between TX and TN

Source: [53].

2.6. Trend Analysis

2.6.1. Mann Kendall Trend Test

The trend analysis is the most often used approach for detecting long-term changes in time series data. Among the several available approaches, researchers typically employ the Mann-Kendall (MK) test and Sen.'s slope test. Mann-Kendall is a non-parametric statistical test used in several research to discover monotonic trends and assess the importance of time series data trends [2, 30]. Identifying a major trend Data analysis were done using Rstudio program [20, 31, 63].

The MK test statistic 'S' is calculated based on [24, 31, 63] using the formula: -

$$S = \sum_{i=1}^{n-1} \sum_{j=i+1}^{n} sgn(x_j - xi) \quad (2)$$

The application of trend test is done to a time series Xi that is ranked from i ¼ 1, 2 … n-1 and Xj, which is ranked from j ¼ i þ 1, 2 …. n. Each of the data point Xi is taken as a reference point, which is, compared with the rest of the data point's Xj so that:

$$sgn(x_j - x_i) = \begin{cases} +1 \;\; if \;\; (xj - xi) > 0 \\ 0 \;\; if \;\; (xj - xi) = 0 \\ -1 \;\; if \;\; (xj - xi) < 0 \end{cases} \quad (3)$$

Where Xi and Xj are the annual values in years i and j (j > i) respectively. It has been documented that when the number of observations is more than 10 (n 10), the statistic 'S' is approximately normally distributed with the mean and E(S) becomes 0 [24].

2.6.2. Sen.'s Slope Estimator

Several authors [43] have used Sen.'s slope estimator [51] method to determine the magnitude of slopes. This method, which assumes a linear trend in the time series, begins by calculating slopes (Z_) of all data pairs using Equation 8.

$$Zi = \frac{Xi - Xk}{i - k} \;\; for, i = 1,2,3 \ldots, N \quad (4)$$

In Equation (4), *N* is the number of data points; Xi and X*k* are observed data values at time *i* and *k* (*i k*), respectively.

The median of these *N* values of Z*i* is the Sen.'s estimator of slope. It is calculated using Equation (5);

$$\beta = \begin{cases} Z_{\frac{N+1}{2}} & N \;\; is \;\; Odd \\ \frac{1}{2}\left(Z_{\frac{Z}{2}} + Z_{\frac{N+1}{2}}\right) & N \;\; is \;\; Even \end{cases} \quad (5)$$

A positive value of indicates an upward (increasing) trend and a negative value indicate a downward (decreasing) trend in the time series. The significance is determined by Equation (6):

$$C_{a=Z_{1-\frac{a}{2}}} \sqrt{Var(Z_i)} \quad (6)$$

In Equation (6) C_a is the confidence interval,$Z_{1-\frac{a}{2}}$ is obtained from the standard normal distribution table and $Var(Z_i)$ is the variance of the slopes. In this study the confidence interval was computed at a = 0.05 significance level.

2.7. Correlation

The Pearson correlation coefficient is used to assess the association between temperature extremes and global climate indicators (ENSO, SOI, PDO, and IOD) [5]. a simple correlation coefficient of 1.0 and -1.0 denotes a perfect positive (direct) and negative (inverse) linear relationship in temperature extremes with Global climate indices, respectively, whereas a correlation coefficient of 0.0 indicates no association between the variables. Equation (1) provides the Pearson correlation coefficient.

2.8. Data Analysis

In the present study Microsoft excel, CDT (Climate data tool), Climate data bias corrector (CDBC), Arc GIS 10.8, R-studio and climate data operator (CDO) were utilized for analysing data.

3. Results and Discussions

This section compares Global Climate Models and CMIP6 Models ENSEMBLE data to Maximum and Minimum Temperature ENACT data across the Borana Zone of Oromia, southern Ethiopia. The performance of climate models was assessed using data from the years 1985 to 2014. First, the observed climatology is compared to the respective climatological means of the nine model Products. The performance is assessed at the grid point level using a spatial resolution of 0.25 ℅0.25 °.

3.1. Bias Corrections and Statistical Descriptions

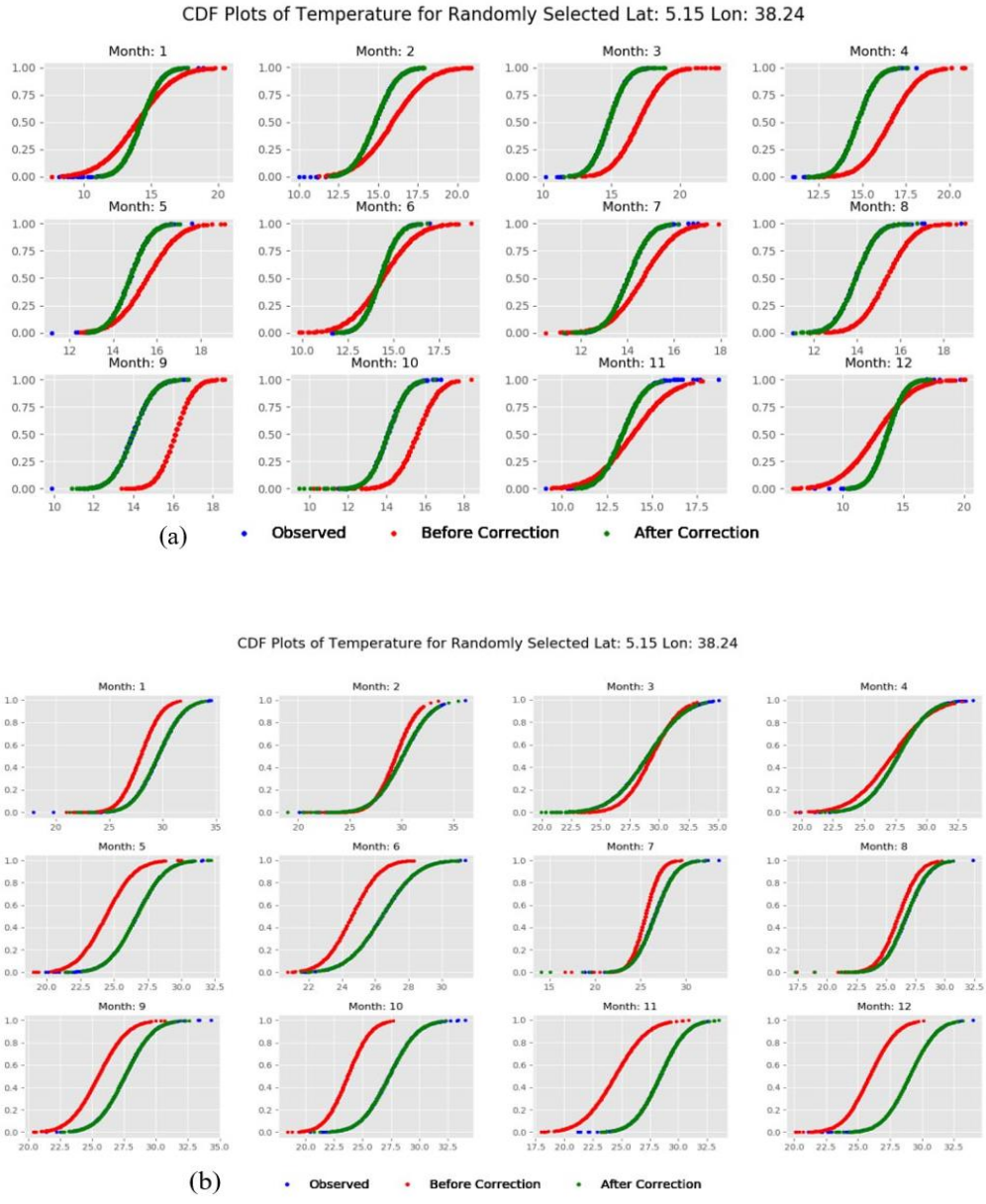
Figure 2 shows the output of a climate data bias corrector tool, which includes two sets of Cumulative Distribution Function (CDF) graphs for temperature from the CNRM model. The (a) figure shows the minimum temperature, while the (b) figure represents the maximum temperature. Both graphs evaluate data for a randomly selected latitude and longitude, illustrating the bias correction methodology's efficiency over the course of a year.

Each subplot in the composite image represents a single month and shows three different CDF curves: observed (blue dots), before correction (red line), and after correction (green

line). The x-axis on these charts commonly reflects temperature in degrees Celsius, while the y-axis shows cumulative probability, which ranges from 0 to 1. The observed data points, which are frequently sparse, indicate the empirical cumulative distribution of real temperature observations during the given month at the stated location. The before Correction curve shows the CNRM model's initial, uncorrected temperature distribution. The after-Correction curve, on the other hand, depicts the temperature distribution of the CNRM model following the use of the bias correction approach.

The major goal of this visualization is to evaluate the effectiveness of the bias correction tool. a successful bias correction would provide an after-correction curve that closely matched the observed data points. In contrast, the Before Correction curve is likely to deviate significantly from the actual data, revealing consistent biases in the raw model output.

The degree of adjustment appears to differ significantly across months and between minimum and maximum temperatures, but the general trend indicates a considerable gain in model fidelity following correction. For example, in some months, the Before Correction curve may regularly overestimate or underestimate temperatures, resulting in a shift to the right or left of the observed data. The after-Correction curve often mitigates these deviations, causing the green line to closely follow the blue dots. This proper alignment is critical for climate impact studies because biased climate model outputs might result in inaccurate estimates of future climatic conditions and their possible effects on diverse sectors.



Note: In Figure 2, the X-axis represents temperature in degrees Celsius and y-axis indicates the cumulative probability

Figure 2. *Cumulative distribution function (CDF) of the minimum (a) and maximum (b) temperatures at Hageremariam station.*

Table 3 illustrates the Mann Kendall Trend Test and Sen.'s Slope Estimator of Temperature Extremes. The results give a strong statistical trend analysis of thirteen temperature-related indices, presenting a clear and compelling narrative of a warming climate. The study efficiently avoids assumptions of data normalcy by using the non-parametric Mann-Kendall test for trend identification [24] and the Theil-Sen estimator for assessing trend size [51], making the findings especially reliable for hydro-climatological data. The indices, most likely from the Expert Team on Climate Change Detection and Indices (ETCCDI), provide a consistent framework for assessing changes in temperature extremes [23, 52, 54, 58].

The most notable aspect of the findings is the robust, statistically significant movement away from cold extremes. The frequency of cool evenings (TN10p) is significantly decreasing (Z = -3.78, p = 0.0002), indicating that nights with extremely low temperatures are becoming increasingly infrequent. This is accompanied by a significant Shorter cold period (CSDI, Z = -2.67, p = 0.0076). These data suggest a significant decrease in the severity and length of winter conditions. Concurrently, the analysis shows a considerable amplification of warm extremes. The frequency of warm nights (TN90p) has grown at a highly significant rate (Z = 3.35, p = 0.0008), indicating human climate change. This warming is not restricted to frequency, but also to intensity, with both the warmest monthly maximum temperature (TXx, Z = 2.98) and the warmest monthly lowest temperature (TNx, Z = 3.30) showing significant increases. Furthermore, the significant increase in Tropical Nights (TR, Z = 2.75) and warm days (TX90p, Z = 2.11) indicates a broad-based warming pattern that affects both daytime and nighttime temperatures.

The findings show signs of asymmetric warming, with nighttime temperatures rising faster than midday temperatures. This is seen by the higher statistical significance of the minimum temperature indices (TN10p, TN90p, TNn, and TNx) compared to their maximum temperature equivalents (TX10p, TX90p, TNn, and TXx). The decreasing, if not statistically significant, trend in the Diurnal Temperature Range (DTR, p = 0.0633) is consistent with this pattern, as a smaller gap between daily high and low temperatures is a well-documented effect of global warming. As a whole, the statistical data largely points to a climate that is not just warming on average but also witnessing a fundamental shift in its extremes, typified by fewer and milder cold occurrences and more frequent and severe heat events, particularly at night.

Table 3. *Mann Kendall Trend Test and Sen.'s Slope Estimator of Temperature Extremes for ENACTS and Selected CMIP6 Models.*

Index	Z(MK)-statist	P-value	Sen's Slope
CSDI	-2.67	0.0076*	-0.0313
DTR	-1.86	0.0633	-0.012
SU	1.57	0.1164	0.6154
TN10p	-3.78	0.0002*	-0.3636
TN90p	3.35	0.0008*	0.3354
TNn	2.66	0.0078*	0.0244
TNx	3.30	0.0010*	0.0388
TX10p	-0.99	0.3176	-0.1018
TX90p	2.11	0.0353*	0.2038
TXn	-1.43	0.1535	-0.0543
TXx	2.98	0.0029*	0.0389
WSDI	1.87	0.0615	0.0035

3.2. Performance of Nine GCM Models in Simulating Minimum and Maximum Temperatures

Table 4 ranks CMIP6 models' ability in replicating monthly average maximum temperature using CORR, ME, MAE, RMSE, and IOA, from 1 (best) to 9 (weakest). INM_CM4 is the top performer (Rank 1), demonstrating excellent accuracy and agreement. It has the highest CORR (0.876), BR2 (0.767), and IOA (0.934), as well as the lowest MAE (16.9) and RMSE (20.775). CNRM (Rank 2) and MPI (Rank 3) both perform quite well, with high CORR (0.841 and 0.837) and IOA (0.914 and 0.912), respectively. INM_CM5 (Rank 4) is likewise quite capable.

Most models have Mean Error (ME) values close to zero, indicating a low level of systematic bias in their highest temperature projections. Miroc_ES2L (Rank 9) and CMC (Rank 8) had poorer performance, with lower CORR and IOA and higher MAE and RMSE.

Table 4. *Using CMIP6 models to simulate the Maximum temperature in the study area.*

Name	CMCC	CNRM	INM_CM4	INM_CM5	Miroc_ES2L	Miroc6	MPI	MRI	NorESM2
CORR	0.766	0.841	0.876	0.834	0.717	0.809	0.837	0.788	0.788
ME	-0.014	0.005	-0.006	0.007	-0.004	-0.004	0	-0.007	0.004
MAE	21.96	19.01	16.9	18.5	26.4	19.7	18.09	21.97	21.8

Name	CMCC	CNRM	INM_CM4	INM_CM5	Miroc_ES2L	Miroc6	MPI	MRI	NorESM2
RMSE	28.954	23.616	20.775	23.974	33.324	25.863	23.72	27.483	27.63
IOA	0.872	0.914	0.934	0.91	0.842	0.897	0.912	0.885	0.886
Rank	8	2	1	4	9	5	3	7	6

The bold Numbers in the Table 4 shows the best performed GCM models in the Simulation of Maximum temperature.

Table 5 compares CMIP6 models for monthly average minimum temperature simulations using CORR, ME, MAE, RMSE, and IOA, as well as an overall ranking. CNRM consistently scores first (1), displaying excellent performance across various parameters, including the greatest CORR (0.835) and IOA (0.912), with low MAE (0.647) and RMSE (0.889). INM_CM5 is a close second (Rank 2), with high competitive scores in all criteria (for example, CORR 0.832, IOA 0.91). MPI (Rank 3) and INM_CM4 (Rank 4) both perform admirably, with MPI having the highest CORR (0.84). Importantly, most models have Mean Error (ME) values close to zero, indicating no systematic bias in their long-term forecasts. CMCC, INM_CM4, INM_CM5, and MPI, for example, have MEs of 0 or 0.001. Miroc_ES2L (Rank 7) and Miroc6 (Rank 8) have usually lower performance, particularly in CORR, MAE, and RMSE. CMCC ranks last (9). The most robust models for minimum temperature simulation are CNRM and INM_CM5, which provide excellent accuracy and strong agreement.

Table 5. *Statistics of Monthly average minimum temperature.*

Name	CMCC	CNRM	INM_CM4	INM_CM5	Miroc_ES2L	Miroc6	MPI	MRI	NorESM2
CORR	0.79	0.835	0.823	0.832	0.794	0.794	0.84	0.82	0.801
ME	0	0.001	0	0	0	-0.004	0	-0.01	0.004
MAE	0.74	0.647	0.663	0.657	0.775	0.761	0.68	0.68	0.735
RMSE	1.01	0.889	0.919	0.896	1.011	1.011	0.92	0.94	0.991
IOA	0.88	0.912	0.905	0.91	0.889	0.889	0.91	0.90	0.89
Rank	9	1	4	2	7	8	3	5	6

The bold Numbers in the Table 5 shows the best performed GCM models in the Simulation of minimum temperature.

3.3. Spatiotemporal Variation of Temperature Extremes over the Study Area

Figure 3 depicts the mean temperature climatology over the Borana Zone, contrasting historical mean temperatures with projected mean temperatures for the mid-century (MID) and far-century (Far) periods under two Shared Socioeconomic Pathways (SSPs): ssp2-4.5, a moderate emissions scenario (MID_ssp2.45, Far_ ssp2-4.5), and ssp5-8.5, a high emissions scenario (MID_ ssp5-8.5 in green, Far_ ssp5-8.5 in dark blue).

A continuous and considerable warming trend is seen across all stations, with all future estimates indicating large rises above the historical baseline (19.8 ℃ to 23.1 ℃). Generally, the ssp5-8.5 scenario causes more warming than ssp2-4.5 for the same period and far-century forecasts are warmer than mid-century projections within the same SSP.

The most extreme warming is expected under Far_ ssp5-8.5, with temperatures in some areas, such as Ebilalo (28.9 ℃) and Aleweya (28.2 ℃), potentially rising by 6-7 ℃ above historical levels. For example, MID_ ssp2-4.5 expects temperatures mostly between 22.5 ℃ and 26 ℃, while Far_ ssp2-4.5 predicts temperatures ranging from 23.3 ℃ to 28.4 ℃. MID_ ssp5-8.5 (blue) typically indicates temperatures between 23.2 ℃ and 26.5 ℃. However, there are substantial contradicting estimates: at Yabello station, the MID_ ssp5-8.5 (23.2 ℃) is projected to be cooler than the MID_ ssp2-4.5 (23.8 ℃).

Furthermore, at the Teltele station, the Far_ ssp2-4.5 projection (28.4 ℃) is significantly higher than the Far_ ssp5-8.5 projection (28.1 ℃). In comparison to many other stations, Yabello's Far_ ssp2-4.5 (25.8 ℃) and Far_ ssp5-8.5 (26.3 ℃) forecasts differ by only 0.5 ℃. In contrast, a feasible outcome is observed at Ebilalo, where Far_ssp2-4.5 (27.0 ℃) is warmer than MID_ ssp5-8.5 (about 26.5 ℃), demonstrating how a far-century moderate scenario might outperform a mid-century high scenario. These extensive and considerable temperature rises, together with individual station anomalies, emphasize

the Borana Zone's complex and severe warming issues, which are anticipated to have an impact on water resources, agriculture, and living conditions. In general, according to this study the Mean Temperature of Borana Zone will increase by 1.57 ℃ and 2.4 ℃ for Near Future SSP2.45 and Near Future SSP5.85 Respectively and also 3.323 ℃ and 3.603 ℃ for Far Future SSP2.45 and Far Future SSP5.85 Respectively.

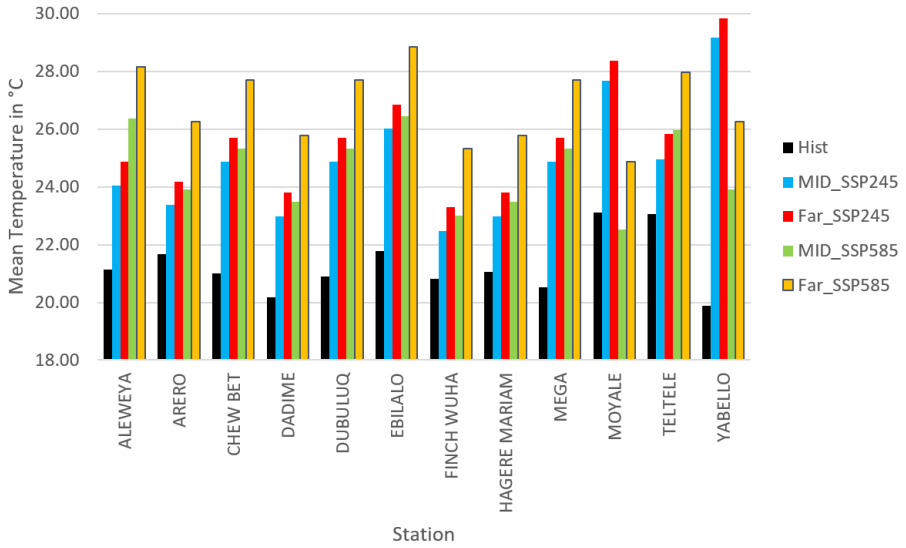


Figure 3. *Mean Temperature Climatology from Historical, Near Future NF (MID) and Far Future (FF) Over Borana Zone.*

Figures 4 and 5 shows the spatial characteristics of DTR in Historical and Future periods over Borana Zone. The diurnal temperature range (DTR), defined as the difference between the daily maximum and minimum temperatures, is a crucial climatic variable influencing ecosystems, hydrological cycles, human health, and agricultural productivity [1]. This essay provides a comparative analysis of the spatial characteristics of historical DTR over the Borana Zone, as depicted in Figure 4 with its near-future (NF) and far-future (FF) projections under various climate change scenarios, as illustrated in Figure 5. The comparison reveals notable shifts in both the magnitude and spatial distribution patterns of DTR. Historically, the Borana Zone exhibited a distinct spatial pattern in its DTR (Figure 4). The region generally experienced a DTR predominantly within the 10-16 ℃ range across its central and northern parts. However, the southern and southwestern regions consistently displayed significantly higher DTR values, frequently reaching 16-18 ℃ and even extending to 18-20 ℃, as evidenced by multiple climate models and observational data (CNRM and INM_CM4 in Figure 4). This historical variability suggests that the southern Borana Zone was characterized by more pronounced daily thermal fluctuations, likely influenced by local topography, land cover, and atmospheric conditions.

In stark contrast to the historical observations, future projections for the Borana Zone consistently indicate a general reduction in the magnitude of DTR across most scenarios and models (Figure 5). Under the CNRM model, near future (NF) and far-future (FF) scenarios for both ssp2-4.5 and ssp5-8.5 project DTR values that are substantially lower than historical peaks. For instance, the NF ssp2-4.5 scenario shows DTRs predominantly between 0-9 ℃, with maximum values around 9-12 ℃ in the south (Figure 5, CNRM NF ssp2-4.5). Similarly, the INM_CM4 model's projections for both NF and FF under ssp2-4.5 and ssp5-8.5 scenarios also present DTR values that rarely exceed 9-10 ℃ (Figure 5, INM_CM4 panels). This widespread decrease in DTR magnitude aligns with global observations of "diurnal temperature range compression," where minimum temperatures have often risen faster than maximum temperatures, leading to a narrower daily temperature window. [7]

Despite the significant reduction in magnitude, the spatial distribution pattern of DTR is projected to largely persist in the future. Both the CNRM and INM_CM4 models, across various scenarios, continue to indicate that the relatively higher DTR values within the future ranges will still be concentrated in the southern and southwestern parts of the Borana Zone, while lower DTRs remain characteristic of the northern and central areas (Figure 5, All Panels). For example, while the historical DTR in the south could reach 18-20 ℃, the future projections show these areas experiencing the highest DTRs of 9-12 ℃ (CNRM FF ssp5-8.5) or 8.6-9 ℃ (INM_CM4 FF ssp5-8.5) within their respective future ranges. This suggests that the underlying geographical factors influencing the spatial heterogeneity of DTR will continue to exert an influence, albeit on a compressed scale. [58].

Variability exists between the projected scenarios. The higher emission pathway, ssp5-8.5, generally projects slightly higher DTR values compared to the lower emission pathway, ssp2-4.5, for both the CNRM and INM_CM4 models (Figure

5 comparing ssp2-4.5 and ssp5-8.5 for each model). However, even these elevated DTRs under SSP5.85 are typically still below the maximum DTR values observed historically. This indicates that irrespective of the future emission trajectory, the Borana Zone is likely to experience a climatic shift towards a reduced daily temperature amplitude compared to its past.

In general, a comparative analysis of historical and projected DTR over the Borana Zone reveals a compelling trend of DTR compression. While the geographical gradient, with higher DTRs in the south, is largely maintained, the absolute magnitude of the DTR is projected to decrease significantly in both the near and future. This consistent finding across multiple climate models and emission scenarios underscores a fundamental alteration in the region's daily thermal regime. Such a shift could have profound implications for agricultural practices, water resource management, biodiversity, and human adaptation strategies in the Borana Zone [59].

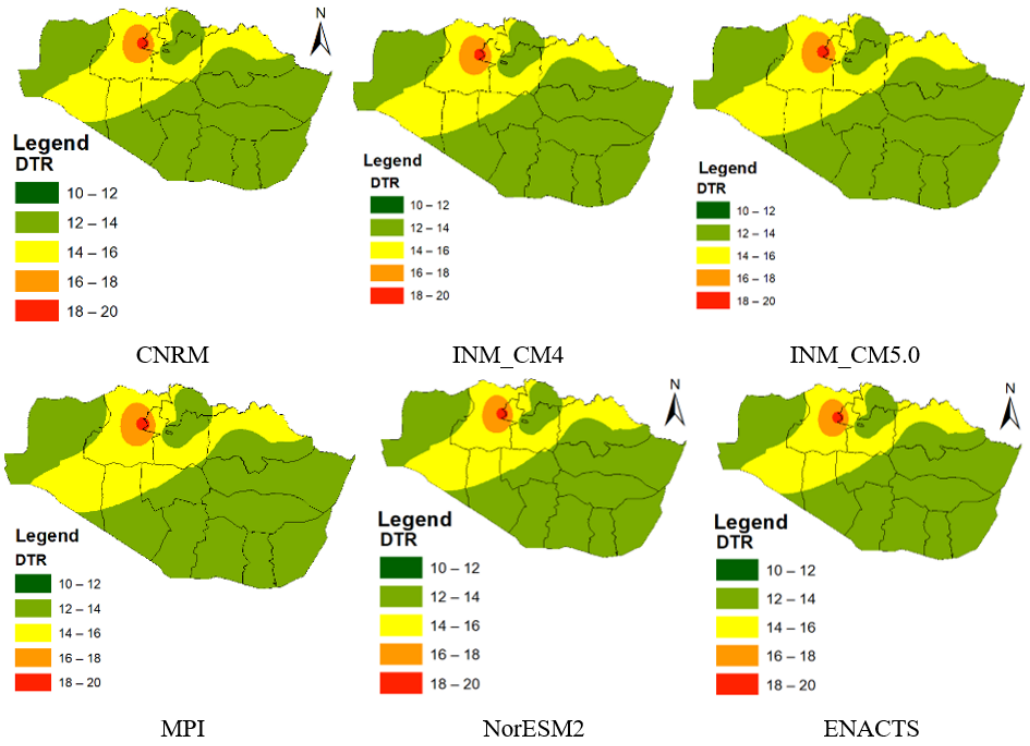


Figure 4. *Spatial characteristics of Historical Diurnal Temperature Range (DTR) over Borana Zone.*

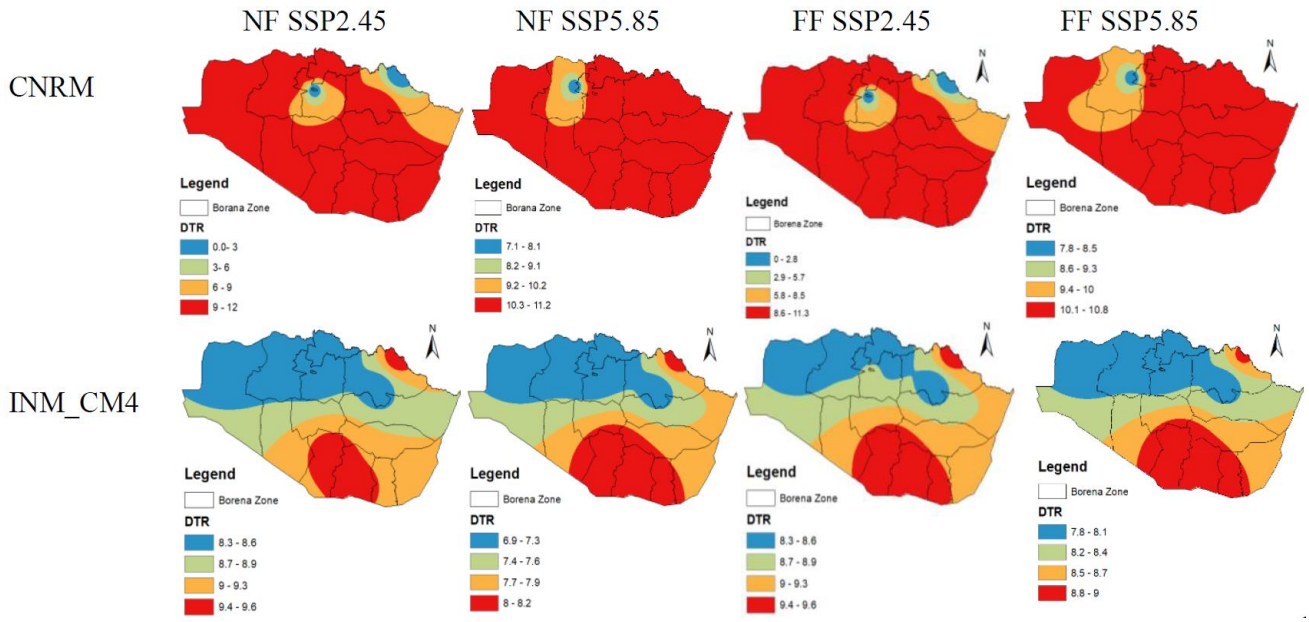


Figure 5. *Spatial characteristics of NF and FF Diurnal Temperature Range (DTR) over Borana Zone.*

The Figure 6 below illustrates the diurnal temperature range (DTR) at Chewbet Station, presenting both historical data and future projections based on CNRM climate models. The DTR, which is the difference between daily maximum and minimum temperatures, is a crucial indicator of climate change impacts, influencing various environmental and biological processes.

Historically, from 1985 to 2014, the DTR at Chewbet Station appears to fluctuate, generally ranging between 12 and 13 ℃. A clear downward trend is visible in the historical data, indicated by the dashed blue Linear (Historical) line, suggesting a decreasing DTR over this period. This observed decline in DTR is a typical global phenomenon, often linked to reasons such as increased cloud cover, urbanization, and rising greenhouse gas concentrations, which tend to warm minimum temperatures more significantly than maximum temperatures [4].

Future forecasts, beginning in 2041 and continuing until 2100, are offered under various Shared Socioeconomic Pathways (SSPs): mid ssp2-4.5, mid ssp5-8.5, Far ssp2-4.5, and Far ssp5-8.5. These SSPs model several future scenarios for greenhouse gas emissions, land use, and other climate change drivers. The estimates consistently show a greater decline in DTR compared to historical values, with temperatures ranging from 10 to 11 ℃ and occasionally falling below 10 ℃. The mid ssp2.45 and Far ssp2.45 scenarios, which likely represent more moderate emission routes, have DTR values that range from 10 to 11 ℃, with minor volatility. The mid ssp5.85 and Far ssp5.85 scenarios, which represent higher emission paths, similarly exhibit DTR values in a similar range, though with slightly different patterns or magnitudes of volatility.

The overall trend across all future possibilities is a sustained drop in DTR, which confirms the pattern seen in previous data. This projected decline in DTR could have various implications, including changed hydrological cycles, effects on agricultural output, and changes in species distribution caused by different temperature conditions [10].

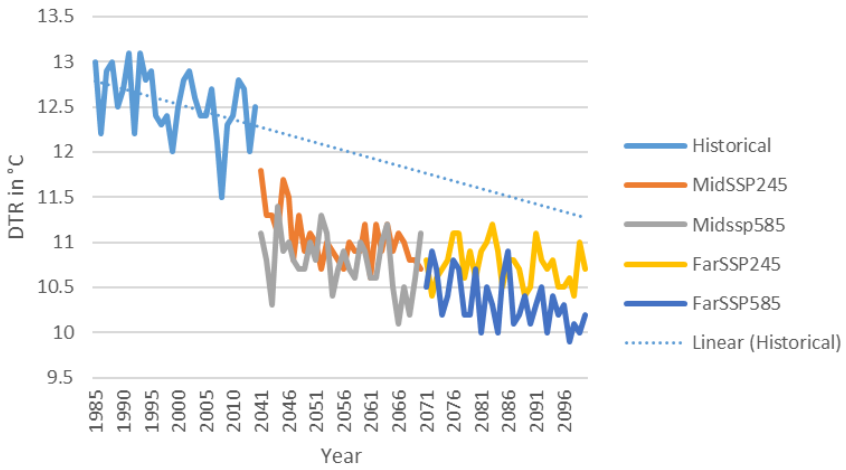
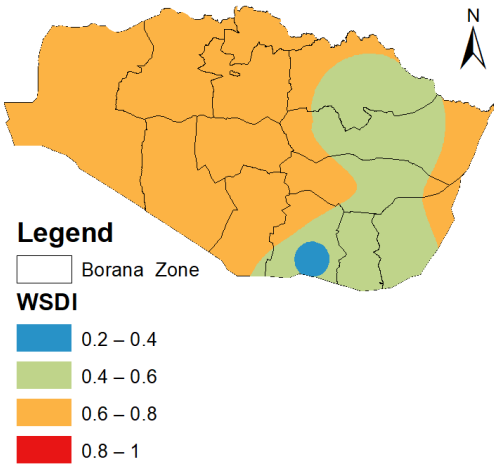


Figure 6. *Trend of Diurnal Temperature Range at Chewbet Station Historical and Future CNRM Data.*

Figure 7 depicts the spatial variation of the historical warm spell duration index (WSDI) over the research area. The WSDI values range from 0.2 to 0.8 days per year, with 0.6 to 0.8 days covering the majority of the Borana zone, 0.4-6 days per year representing the eastern half of the west zone, and less than 0.4 days per year in the southeast. Figure 8 depicts the WSDI projections for the near and far future under two alternative climatic scenarios. SSP2-4.5 is a moderate scenario, and ssp5-8.5 is a high-emission scenario. NF SSP2-4.5 results in a considerable rise in WSDI (0.43 - 0.87) as compared to the baseline. The WSDI values in NF ssp5.85 are substantially higher (0.63 - 0.93), suggesting that a high-emissions pathway significantly accelerates the increase in heatwave duration.

The top range indicates that some places may experience heatwave conditions for the bulk of the year. In the FF ssp2-4.5, WSDI values (0.63 - 0.8) are severe and correspond to the worst Near-Future scenario. Extreme rises in WSDI have serious consequences for human health, agricultural production, and ecological resilience. [35] FF ssp5-8.5. This projection is troubling. WSDI readings ranging from 0.93 to 1.2 indicate that the climate is undergoing total transition. The value of 1.2 indicates that the number of days in heatwave surpasses the number of days in a year, meaning that heatwave is not only persistent but also increasing in overlap and frequency. This symbolizes a new normal of continuous high temperatures.



Historical

Figure 7. *Historical Distribution of Warm Spell Duration Index Using CNRM Model on Borana Zone.*

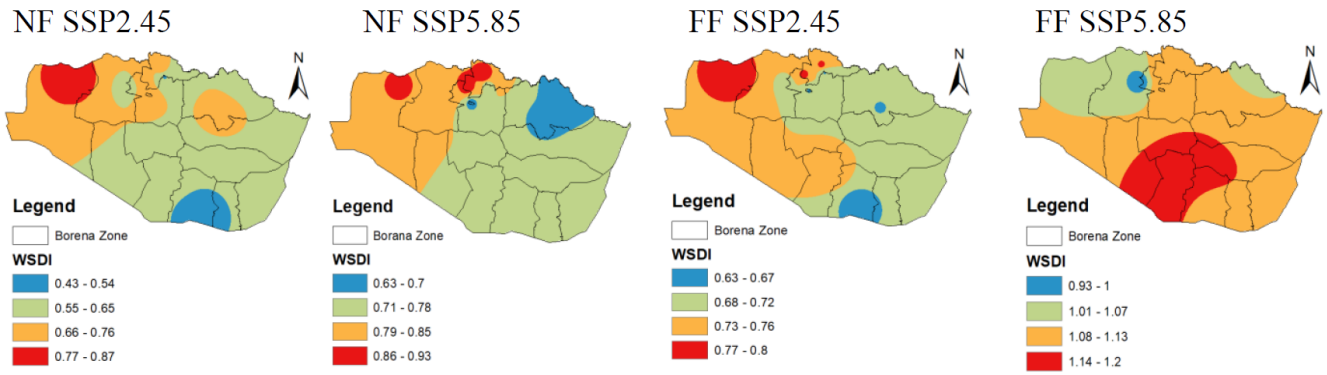


Figure 8. *Spacial Variation of WSDI in Near Future and Far Future over the Study Area.*

Figure 9 depicts the WSDI Trend in Days/Year for the Chewbet station, providing a historical baseline. This historical period has high inter-annual variability in warm spells, defined as at least six consecutive days with maximum temperatures surpassing the 90th percentile for that calendar day. [10]. Many years in the historical record have a WSDI of zero, suggesting the absence of such extended warm episodes. However, there are periodic rises, most notably around the year 2000, with around 4 days each year, and again around 2011, with approximately 3 days per year. These spikes illustrate episodic occurrences of significant warm periods within a historically low average, which has typically remained below one day per year.

This historical variability emphasizes the natural oscillations in regional climate, against which future estimates must be measured. All future scenarios consistently show an increase in WSDI relative to the historical baseline, indicating the possibility of more frequent and/or longer warm periods [29]. The extent of this expected increase, however, is greatly dependent on the emissions scenario (SSP pathway) and time period. The moderate emissions scenario (ssp2.45) predicts a small increase in WSDI between 2041 and 2070. Values in this scenario typically range between 0 and 3 days per year, with a linear trend (dotted line) indicating a progressive rise of 0.5 to 1 day each year.

This middle-of-the-road scenario predicts that warm periods will become slightly more common, but their increase will be substantially restricted if moderate mitigation actions are adopted. [42].

In comparison, the high emissions scenario (ssp5-8.5) predicts a more significant increase in WSDI by mid-century. Values in this scenario typically exceed one day per year, with noticeable increases of up to five days per year (around 2065, 2068). This suggests that if emissions continue to rise, warm spells will become significantly longer and/or more frequent by mid-century, offering increased adaptation issues.

The disparity between emissions scenarios becomes considerably more pronounced in long-term estimates (2071-2100). Under the moderate emissions scenario (ssp2-4.5), the WSDI continues to rise, ranging from zero to 2-3 days each year.

The linear trend implies a small increase that could average 1 to 1.5 days per year by the end of the century. This implies that even with moderate emissions, the persistence of warm spells will remain an issue. However, the high emission scenario (SSP5-8.5) predicts a significant and frightening increase in WSDI. Values in this scenario typically exceed two

days per year, with large surges exceeding six days per year (around 2093, 2098). If greenhouse gas emissions continue at current levels, this scenario predicts significantly longer and more frequent warm spells by the end of the century.

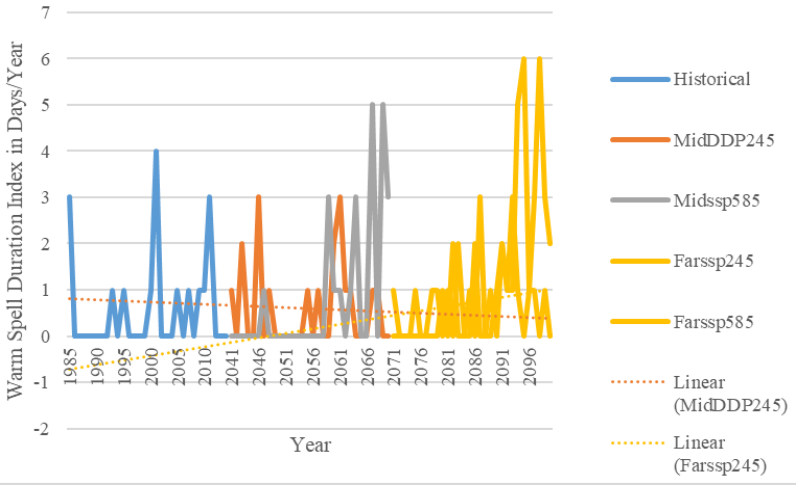


Figure 9. *Trend of WSDI in Chewbet station from Historical to Projection periods Using CNRM Model.*

3.4. Relation of Temperature Extremes with Large-scale Climate Indices over the Study Area

Table 6 illustrates the association between temperature extremes and large-scale climate indices the link between temperature extremes and large-scale climate indicators is an important field of research in climate science, providing insights into the mechanisms that drive regional climate variability. Table 6 shows a complicated web of relationships between numerous climate extreme indices and key global climate models including ENSO, PDO, and IOD. The El Niño-Southern Oscillation (ENSO), represented by the Southern Oscillation Index (SOI) and the NINO3.4, SST anomaly, exhibits a fundamental inverse relationship.

The significant negative association between high SOI values (indicating La Niña) and cooler NINO3.4 temperatures is key to understanding ENSO. [48] ENSO has a noticeable impact on temperature extremes, albeit with varying degrees. El Niño conditions may be linked to longer or more frequent cold spells, as indicated by a slight positive association between NINO3.4 and the Cold Spell Duration Index (0.24). NINO3.4 has a weak to moderate negative association (-0.30) with the Warm Spell Duration Index (WSDI), suggesting that El Niño may result in shorter or fewer warm spells. [21] The Diurnal Temperature Range (DTR) has a weak negative connection with SOI (-0.28), potentially due to increased cloudiness and precipitation during La Niña occurrences. [33].

The Indian Ocean Dipole (IOD) significantly influences temperature extremes, especially in places affected by Indian Ocean dynamics. The positive IOD phase shows a somewhat positive correlation with Summer Days (SU) (0.40), showing a link to a higher frequency of summer days. Furthermore, a moderate negative connection with TN10P (% of cold nights) (-0.42) indicates that a positive IOD phase is connected to fewer cold nights [47].

However, the IOD's correlations with spell durations (CSDI: -0.14, WSDI: -0.08) are generally weak in this dataset, indicating that it has a less direct influence on the overall length or frequency of cold and warm spells than ENSO or PDO.

Table 6. *Correlation between Temperature Extremes and Large-Scale Climate Indices.*

Index	CSDI	DTR	SU	TN10P	TN90P	TNn	TNx	TR	TX10P	TX90P	TXn	TXx	WSDI	AMO	PDO	IOD	SOI	NINO3.4
CSDI	1.0																	
DTR	0.2	1.0																
SU	-0.2	0.6	1.0															
TN10P	0.9	0.1	-0.5	1.0														
TN90P	0.2	0.2	0.6	-0.1	1.0													

Index	CSDI	DTR	SU	TN10P	TN90P	TNn	TNx	TR	TX10P	TX90P	TXn	TXx	WSDI	AMO	PDO	IOD	SOI	NINO3.4
TNn	-0.7	0.0	0.2	-0.6	-0.2	1.0												
TNx	0.2	0.3	0.6	0.0	0.9	-0.4	1.0											
TR	0.3	0.2	0.5	0.0	0.6	-0.3	0.8	1.0										
TX10P	0.3	-0.6	-0.9	0.5	-0.5	-0.2	-0.5	-0.4	1.0									
TX90P	0.1	0.7	0.8	-0.2	0.7	0.0	0.7	0.5	-0.7	1.0								
TXn	-0.1	0.4	0.5	-0.2	0.4	0.2	0.3	0.2	-0.6	0.4	1.0							
TXx	0.0	0.4	0.5	-0.1	0.7	0.0	0.7	0.5	-0.5	0.7	0.5	1.0						
WSDI	0.0	0.6	0.6	-0.2	0.6	0.1	0.4	0.2	-0.5	0.9	0.5	0.5	1.0					
AMO	0.1	-0.1	0.2	-0.1	0.4	-0.2	0.3	0.1	-0.2	0.1	0.3	0.3	0.0	1.0				
PDO	-0.1	-0.1	-0.2	0.0	-0.3	0.3	-0.4	-0.3	0.3	-0.1	-0.4	-0.4	0.0	-0.5	1.0			
IOD	0.0	0.0	0.3	-0.1	0.5	-0.3	0.4	0.1	-0.2	0.3	0.2	0.2	0.3	0.6	-0.1	1.0		
SOI	0.4	-0.1	-0.1	0.3	0.2	-0.2	0.3	0.2	0.1	-0.1	0.3	0.2	-0.1	0.4	-0.6	-0.1	1.0	
NINO3.4	-0.3	0.2	0.3	-0.3	0.1	0.1	0.1	0.1	-0.3	0.3	-0.1	0.0	0.2	-0.1	0.5	0.4	-0.9	1.0

Figure 10 depicts the spatial correlation coefficients of two major climate drivers, the Atlantic Multidecadal Oscillation (AMO) and the Indian Ocean Dipole (IOD), as well as key temperature extreme indices such as the Cold Spell Duration Index (CSDI), Diurnal Temperature Range (DTR), Cool Nights (TX10p), and Warm Spell Duration Index (WSDI). This analysis demonstrates unique but complicated teleconnections that highlight the interdependence of global climate processes and local weather patterns.

The AMO, represented in the left panels, has a subtle influence on temperature extremes throughout the Borana zone. For example, the occurrence of strong negative correlations with TX10p (cold nights) in some sub-regions indicates a decrease in the frequency or severity of cool nights during specific phases of the AMO, signifying a warmer nocturnal environment [34]. In contrast, positive associations with WSDI (warm spells) in other locations imply a higher risk of lengthy periods of high temperatures. The varied spatial distribution of these relationships for CSDI and DTR demonstrates that the AMO's effect on cold spells and daily temperature fluctuation is not uniform, but rather geographically variable.

Similarly, the IOD, as shown in the right panels, leaves its own unique impression on the temperature extremes of the Borana Zone. Significant positive relationships with WSDI in some locations hint to an increase in warm spell lengths, which may exacerbate heat-related difficulties [45]. Conversely, negative associations with TX10p in other places indicate fewer cool nights, adding to an overall warming trend in nocturnal temperatures. The regionally heterogeneous patterns obtained for CSDI and DTR under IOD impact highlight the region's distinct vulnerability to cold extremes and daily temperature changes based on IOD phase.

Figure 10 reveals considerable geographic variation in correlation patterns for both AMO and IOD over the Borana Zone. This variability is an important result, demonstrating that the remote forcing from these oceanic oscillations is locally mediated by a variety of factors such as regional topography, land-surface interactions, and complex atmospheric circulation anomalies [26]. Such localized responses demand climate adaptation techniques that are personalized rather than generic. The ability to link large-scale climate indices to specific local extreme events is extremely useful for refining seasonal to decadal climate forecasts, improving early warning systems for heatwaves and cold snaps, and informing climate-resilient development planning in vulnerable communities [8].

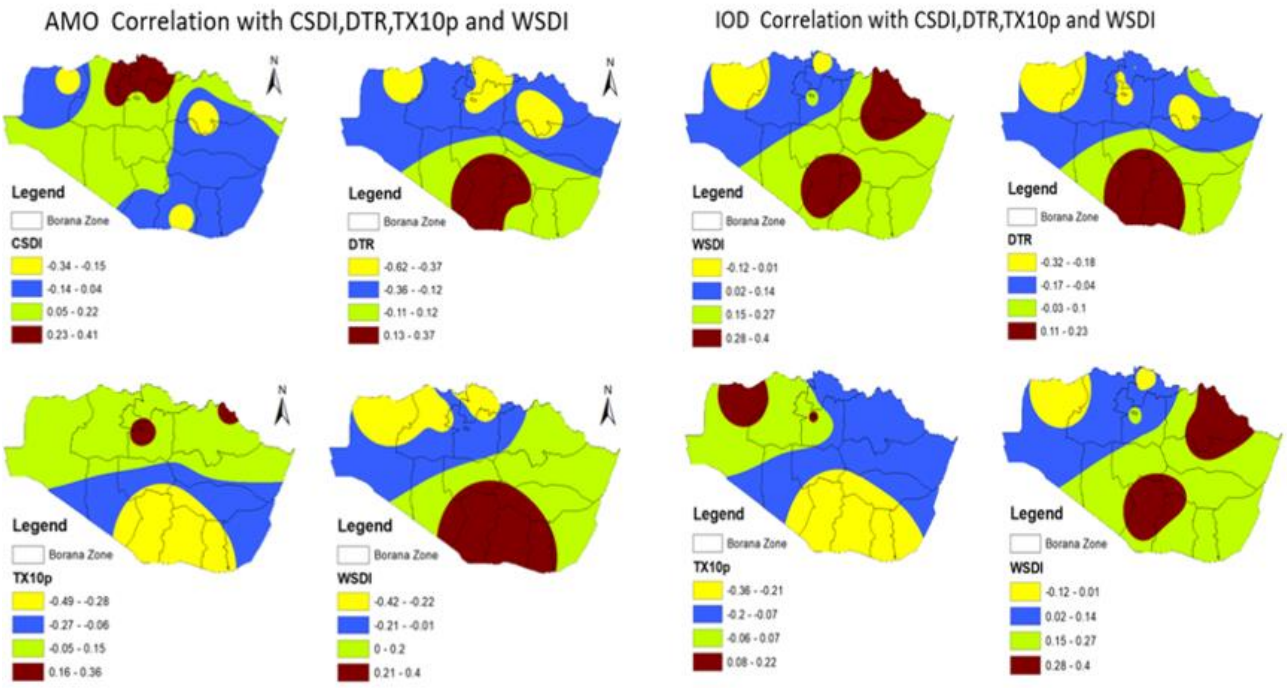


Figure 10. *Spatial correlation coefficients of AMO (Left) and IOD (Right) with Temperature Extremes.*

Figure 11 shows the geographic correlation coefficients between the El Niño-Southern Oscillation (ENSO), represented by the Niño 3.4 index, and the Pacific Decadal Oscillation (PDO), with selected temperature extreme indices in the Borana Zone. These indices are the Cold Spell Duration Index (CSDI), Diurnal Temperature Range (DTR), Cool Nights (TX10p), and Warm Spell Duration Index (WSDI). The left panels show the Niño 3.4 correlations, whereas the right panels show those for the PDO. This thorough mapping sheds light on the complex teleconnections that link distant marine occurrences to localized temperature extremes.

The Niño 3.4 index, a fundamental indication of ENSO variability, has a clear impact on temperature extremes in the Borana Zone. Several places have significant negative correlations with TX10p (cold nights), suggesting a decrease in the frequency or duration of cool nights during positive Niño 3.4 phases (El Niño occurrences) [15]. Other locations also show favorable relationships with WSDI (warm spells), indicating a higher proclivity for protracted warm periods during such phases. The different correlations for CSDI and DTR demonstrate that the impact on cold spells and daily temperature range is not uniform, but varies geographically, reflecting the complicated atmospheric responses to ENSO forcing. Furthermore, the PDO, a longer-term climate oscillation in the Pacific, shows clear teleconnections to Borana's temperature extremes. The PDO maps show places with high negative correlations to TX10p, indicating less cool nights during positive PDO phases, which are frequently associated with warmer Pacific conditions [32]. Positive associations with WSDI are found across considerable areas of the zone, indicating an increased risk of warm spells. The spatial patterns of CSDI and DTR correlations under PDO influence highlight the various regional temperature responses to this decadal-scale factor.

Figure 11 reveals significant regional variability in connections between Niño 3.4 and PDO across the Borana Zone. This variability is critical for understanding regional climate dynamics because it shows that the influence of these large-scale oceanic phenomena is not uniformly distributed, but is heavily influenced by local geographical features, land-atmosphere interactions, and complex atmospheric teleconnection pathways [26].

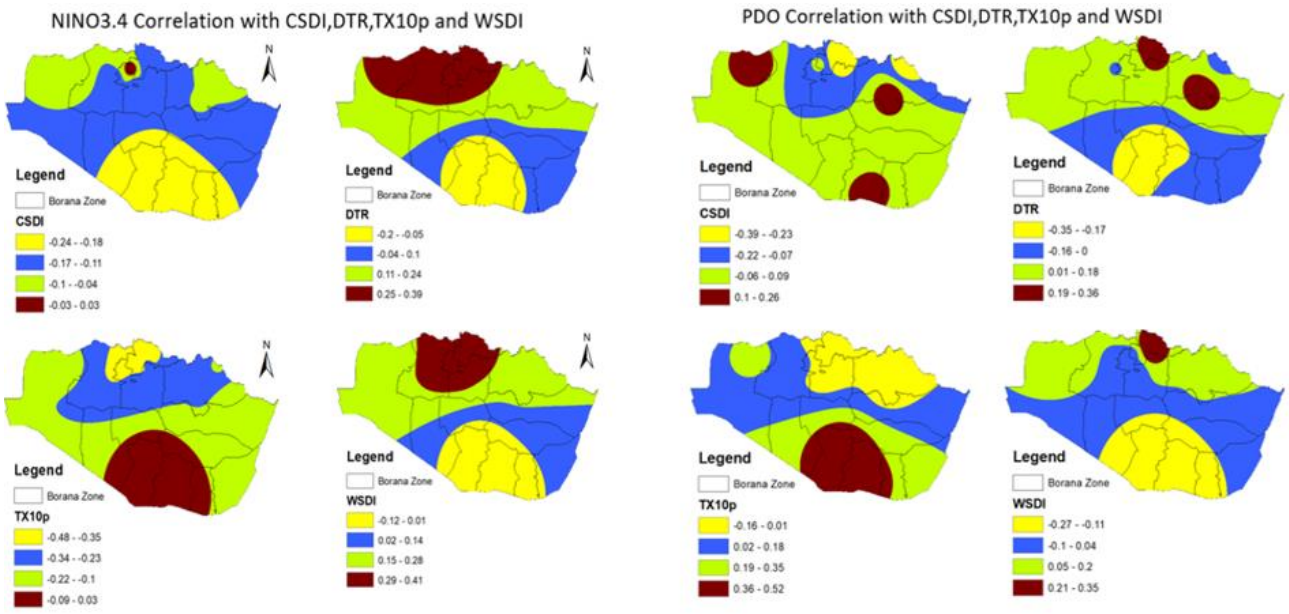


Figure 11. *Spatial correlation coefficients of NINO3.4 (Left) and PDO (Right) with Temperature Extremes.*

4. Conclusion and Recommendations

4.1. Conclusions

This study explored the historical evolution and future trajectory of temperature extremes in the Borana Zone using ENACTS observational datasets [9] and selected CMIP6 climate model simulations [46] under ssp2-4.5 and ssp5-8.5 scenarios [40]. By integrating extreme climate indices, statistical trend analysis, and teleconnection relationships, the research provides a comprehensive assessment of both past climate variability and projected future conditions. The findings reveal a region undergoing pronounced climatic shifts, particularly in temperature extremes, and the frequency of climate-related hazards [62].

Temperature projections show clear warming trends. Warm Spell Duration Index (WSDI) values increase steadily across all models and scenarios, consistent with global increases in heat extremes [12]. By the far future, WSDI intensifies further to 0.63–0.8 under ssp2-4.5 and 0.93–1.2 under ssp5-8.5. The compression of the diurnal temperature range (DTR), declining from 12–13 ℃ historically to 10–11 ℃ in future periods, and sometimes below 10 ℃, is consistent with faster nighttime warming observed globally [39, 58].

The combined evidence from historical trends, model projections, extreme indices, and teleconnection analyses confirms that the Borana Zone is entering a future of heightened climatic variability. Heatwaves will grow in frequency and duration. These changes will have implications for pastoralism, environmental stability across the region.

4.2. Recommendations

Based on the findings of this study, it is recommended that climate adaptation measures be strengthened through improved livestock management, sustainable grazing practices, and enhanced water resource development to reduce the impacts of increasing temperature extremes. Climate monitoring and early warning systems should also be improved by incorporating large-scale climate indices, such as ENSO, PDO, IOD, SOI, and AMO, to enhance the prediction of extreme temperature events. Furthermore, the adoption of climate-smart agricultural and pastoral practices, including drought- and heat-tolerant crop varieties, rangeland restoration, and efficient water conservation techniques, should be promoted. Future climate projections from CMIP6 should be integrated into regional planning and decision-making to support climate-resilient land use, water resource management, and disaster risk reduction. Finally, increasing community awareness and promoting ecosystem restoration through sustainable natural resource management will be essential for improving the resilience of the Borana Zone to future climate change.

Abbreviations

MK	Mann-Kendall
Q	Sen's Slope
CSDI	Cold Spell Duration Index
DTR	Diurnal Temperature Range
ENACTS	Enhanced National Climate Services
IOA	Index of Agreement
SSP	Shared Socio-Economic Pathway
WSDI	Warm Spell Duration Index

Authors Contributions

Mikiyas Gebre Arrefaine: Conceptualization, Data curation, Formal Analysis, Investigation, Methodology, Resources, Software, Visualization, Writing – original draft

Tesfay Mekonnen Weldegerima: Methodology, Resources, Supervision, Validation, Writing – review & editing

Conflicts of Interest

The authors declare no conflicts of interest.

References

[1] Asefa, G., Kebede, A., & Mengesha, M. (2025). Heliyon Changes in climate extreme indices and agricultural drought monitoring in the semi-arid areas of Borana zone, southern Ethiopia. *Heliyon*, *11*(2), e42041. https://doi.org/10.1016/j.heliyon.2025.e42041

[2] Asfaw, A., Simane, B., Hassen, A., & Bantider, A. (2018). Variability and time series trend analysis of rainfall and temperature in northcentral Ethiopia: A case study in Woleka sub-basin. *Weather and climate extremes*, *19*, 29–41.

[3] Ayele, A. G. (2025). *Evaluation and Selection of the CMIP6 Climate Model over*. *9*(2), 90–98.

[4] Azorin-molina, C., & Zeng, Z. (2023). *Increasing Global Terrestrial Diurnal Temperature Range for 1980 – 2021 Geophysical Research Letters*. https://doi.org/10.1029/2023GL103503

[5] Beyene, T. K., Jain, M. K., Yadav, B. K., & Agarwal, A. (2022). Multiscale investigation of precipitation extremes over Ethiopia and teleconnections to large-scale climate anomalies. *Stochastic Environmental Research and Risk Assessment*, *36*(5), 1503–1519. https://doi.org/10.1007/s00477-021-02120-y

[6] Birara, H., Pandey, R. P., & Mishra, S. K. (2018). Trend and variability analysis of rainfall and temperature in the tana basin region, Ethiopia. *Journal of Water and Climate Change*, *9*(3), 555–569. https://doi.org/10.2166/wcc.2018.080

[7] Braganza, K., & Karoly, D. J. (2014). *Diurnal temperature range as an index of global climate change during the twentieth century Diurnal temperature range as an index of global climate change during the twentieth century*. *May*. https://doi.org/10.1029/2004GL019998

[8] Connell, C. O., Aizpurua, E., & Rogan, M. (2021). The European committee for the prevention of torture and the gendered experience of imprisonment. *Crime, Law and Social Change*, *0123456789*. https://doi.org/10.1007/s10611-021-09938-1

[9] Dinku, T., Funk, C., Peterson, P., Maidment, R., & Tadesse, T. (2018). *Validation of the CHIRPS satellite rainfall estimates over eastern*. *June 2017*, 292–312. https://doi.org/10.1002/qj.3244

[10] Easterling, D. R., Horton, B., Jones, P. D., Peterson, T. C., Karl, T. R., Parker, D. E., Salinger, M. J., Razuvayev, V., Plummer, N., Jamason, P., & Folland, C. K. (1997). *Trends for the Globe Emm*. *July*, 18–21.

[11] Enawgaw, A., Asmare, A., Nigussie, B., Tefera, T., & Mihiretie, Y. (2024). Future drought characterization using multiple drought indices and CMIP - 6 Climate Models within Mille Watershed, Lower Awash. *Theoretical and Applied Climatology*, *155*(10), 9367–9390. https://doi.org/10.1007/s00704-024-05188-y

[12] Engelbrecht, F. (2021). *The IPCC Assessment Report Six Working Group 1 report and southern Africa : Reasons to take action*. *117*(11), 1–7.

[13] Eyring, V., Bony, S., Meehl, G. A., Senior, C. A., Stevens, B., Stouffer, R. J., & Taylor, K. E. (2016). Overview of the Coupled Model Intercomparison Project Phase 6 (CMIP6) experimental design and organization. *Geoscientific Model Development*, *9*(5), 1937–1958. https://doi.org/10.5194/gmd-9-1937-2016

[14] Feyissa, T. A., Demissie, T. A., & Saathoff, F. (2023). *Evaluation of General Circulation Models CMIP6 Performance and Future Climate Change over the Omo River Basin, Ethiopia*.

[15] Gleixner, S., Keenlyside, N., Viste, E., & Korecha, D. (2017). The El Niño effect on Ethiopian summer rainfall. *Climate Dynamics*, *49*(5–6), 1865–1883. https://doi.org/10.1007/s00382-016-3421-z

[16] Gonfa, L. (1996). *Climate classifications of Ethiopia*.

[17] Gupta, R., & Bhattarai, R. (2019). *Development of Climate Data Bias Corrector (CDBC) Tool and Its Application over the Agro-Ecological*.

[18] Gurara, M. A., Tolche, A. D., Jilo, N. B., & Kassa, A. K. (2022). Annual and seasonal rainfall trend analysis using gridded dataset in the Wabe Shebele River Basin, Ethiopia. *Theoretical and Applied Climatology*, *150*(1–2), 263–281.

[19] Hessebo, M. T., Woldeamanuel, T., & Tadesse, M. (2021). Spatial and temporal climate variability and change in the bilate catchment, central Rift Valley lakes region, Ethiopia. *Physical Geography*, *42*(3), 199–225. https://doi.org/10.1080/02723646.2019.1698094

[20] Jain, S. K., & Kumar, V. (2012). Trend analysis of rainfall and temperature data for India. *Current Science*, *102*(1), 37–49.

[21] Jones, R., & Lawrence, M. (2018). *Re: Jones et al., Nutrients 2018, 10, 501*. https://doi.org/10.3390/nu10060746

[22] Kebede, Z. A., & Wedajo, G. K. (2025). Jo ur l P re of. *Natural Hazards Research*, *6*. https://doi.org/10.1016/j.nhres.2025.08.006

[23] Keggenhoff, I., Elizbarashvili, M., Amiri-Farahani, A., & King, L. (2014). Trends in daily temperature and precipitation extremes over Georgia, 1971-2010. *Weather and Climate Extremes*, *4*, 75–85. https://doi.org/10.1016/j.wace.2014.05.001

[24] Kendall, K. (1975). Thin-film peeling-the elastic term. *Journal of Physics D: Applied Physics*, *8*(13), 1449.

[25] Kenyon, J., & Hegerl, G. C. (2008). Influence of modes of climate variability on global temperature extremes. *Journal of Climate*, *21*(15), 3872–3889. https://doi.org/10.1175/2008JCLI2125.1

[26] Kijazi, A. L., & Reason, C. J. C. (2009). *Analysis of the 2006 floods over northern Tanzania †*. *970*(January), 955–970. https://doi.org/10.1002/joc

[27] King'uyu, S. M., Ogallo, L. A., & Anyamba, E. K. (2000). Recent trends of minimum and maximum surface temperatures over Eastern Africa. *Journal of Climate*, *13*(16), 2876–2886. https://doi.org/10.1175/1520-0442(2000)013<2876:RTOMAM>2.0.CO;2

[28] Korecha, D., & Barnston, A. G. (2007). Predictability of June-September rainfall in Ethiopia. *Monthly Weather Review*, *135*(2), 628–650. https://doi.org/10.1175/MWR3304.1

[29] Legg, S. (2021). IPCC, 2021: Climate change 2021-the physical science basis. *Interaction*, *49*(4), 44–45.

[30] Manatsa, D., Chingombe, W., & Matarira, C. H. (2008). The impact of the positive Indian Ocean dipole on Zimbabwe droughts Tropical climate is understood to be dominated by. *International Journal of Climatology*, *2029*(March 2008), 2011–2029. https://doi.org/10.1002/joc.1695

[31] Mann, H. B. (1945). Nonparametric tests against trend. *Econometrica: Journal of the econometric society*, 245–259.

[32] Mantua, N. J., & Hare, S. R. (2002). The Pacific Decadal Oscillation. *Journal of Oceanography*, *58*(1), 35–44.

[33] Marjani, S., Alizadeh-Choobari, O., & Irannejad, P. (2019). Frequency of extreme El Niño and La Niña events under global warming. *Climate Dynamics*, *53*(9), 5799–5813. https://doi.org/10.1007/s00382-019-04902-1

[34] Mcdowell, S. (2017). *Preparing for the 2015-2016 El Niño : October*.

[35] Meehl, G. A., Arblaster, J. M., & Tebaldi, C. (2005). *Understanding future patterns of increased precipitation intensity in climate model simulations*. *32*(September), 2–5. https://doi.org/10.1029/2005GL023680

[36] Molla, M. (2020). Teleconnections between Ocean-Atmosphere Coupled Phenomenon and Droughts in Tigray Region: Northern Ethiopia. *American Journal of Climate Change*, *9*(3), 274–296.

[37] New, M., Hewitson, B., Stephenson, D. B., Tsiga, A., Kruger, A., Manhique, A., Gomez, B., Coelho, C. A. S., Masisi, D. N., Kululanga, E., Mbambalala, E., Adesina, F., Saleh, H., Kanyanga, J., Adosi, J., Bulane, L., Fortunata, L., Mdoka, M. L., Lajoie, R., … Town, C. (2006). *Evidence of trends in daily climate extremes over southern and west Africa*. *111*, 1–11. https://doi.org/10.1029/2005JD006289

[38] Nguyen-duy, T., & Desmet, Q. (2023). *Uncorrected Proof Performance evaluation and ranking of CMIP6 global climate models over Vietnam Uncorrected Proof*. *00*(0), 1–16. https://doi.org/10.2166/wcc.2023.454

[39] Nkemelang, T., New, M., & Zaroug, M. (2018). Temperature and precipitation extremes under current, 1.5 C and 2.0 C global warming above pre-industrial levels over Botswana, and implications for climate change vulnerability. *Environmental Research Letters*, *13*(6), 65016.

[40] O'Neill, B. C., Tebaldi, C., Van Vuuren, D. P., Eyring, V., Friedlingstein, P., Hurtt, G., Knutti, R., Kriegler, E., Lamarque, J.-F., & Lowe, J. (2016). The scenario model intercomparison project (ScenarioMIP) for CMIP6. *Geoscientific Model Development*, *9*(9), 3461–3482.

[41] Omondi, P. A. o., Awange, J. L., Forootan, E., Ogallo, L. A., Barakiza, R., Girmaw, G. B., Fesseha, I., Kululetera, V., Kilembe, C., Mbati, M. M., Kilavi, M., King'uyu, S. M., Omeny, P. A., Njogu, A., Badr, E. M., Musa, T. A., Muchiri, P., Bamanya, D., & Komutunga, E. (2014). Changes in temperature and precipitation extremes over the Greater Horn of Africa region from 1961 to 2010. *International Journal of Climatology*, *34*(4), 1262–1277. https://doi.org/10.1002/joc.3763

[42] Pachauri, R. K. (2014). *Climate Change 2014 Synthesis Report*.

[43] Partal, T., & Kahya, E. (2006). Trend analysis in Turkish precipitation data. *Hydrological Processes*, *20*(9), 2011–2026. https://doi.org/10.1002/hyp.5993

[44] Pierce, D. W., Cayan, D. R., Maurer, E. P., Abatzoglou, J. T., & Hegewisch, K. C. (2015). Improved bias correction techniques for hydrological simulations of climate change. *Journal of Hydrometeorology*, *16*(6), 2421–2442.

[45] Res, C., Saji, N. H., & Yamagata, T. (2003). *Possible impacts of Indian Ocean Dipole mode events on global climate*. *25*, 151–169.

[46] Riahi, K., Vuuren, D. P. Van, Kriegler, E., Edmonds, J., Neill, B. C. O., Fujimori, S., Bauer, N., Calvin, K., Dellink, R., Fricko, O., Lutz, W., Popp, A., Crespo, J., Kc, S., Leimbach, M., Jiang, L., Kram, T., Rao, S., Emmerling, J., … Tavoni, M. (2017). *The Shared Socioeconomic Pathways and their energy, land use, and greenhouse gas emissions implications : An overview*. *42*, 153–168. https://doi.org/10.1016/j.gloenvcha.2016.05.009

[47] Saji, N. H., & Yamagata, T. (2014). *Possible impacts of Indian Ocean Dipole mode events on global climate*. *December 2003*. https://doi.org/10.3354/cr025151

[48] Sea, N., Temperature, S., High, S. S., Lin, J., Tang, M., & Wijaya, F. (2022). *Indonesian Journal of Earth Sciences Satellite Oceanographic Data Processing and Analysis : Correlation Between*. *2*(2), 157–176. https://doi.org/10.52562/injoes.v2i2.428

[49] Segele, Z. T., & Lamb, P. J. (2005). Characterization and variability of Kiremt rainy season over Ethiopia. *Meteorology and Atmospheric Physics*, *89*(1–4), 153–180. https://doi.org/10.1007/s00703-005-0127-x

[50] Seleshi, Y., & Demaree, G. R. (1995). Rainfall Variability in the Ethiopian and Eritrean Highlands and its Links with the Southern Oscillation Index. *Journal of Biogeography*, *22*(4/5), 945. https://doi.org/10.2307/2845995

[51] Sen, P. K. (1968). Journal of the American Statistical Estimates of the Regression Coefficient Based on Kendall's Tau. *Journal of the American Statistical Association*, *63*(324), 1379–1389.

[52] Seneviratne, S. I., Nicholls, N., Easterling, D., Goodess, C. M., Kanae, S., Kossin, J., Luo, Y., Marengo, J., Mc Innes, K., Rahimi, M., Reichstein, M., Sorteberg, A., Vera,

[53] C., Zhang, X., Rusticucci, M., Semenov, V., Alexander, L. V., Allen, S., Benito, G., … Zwiers, F. W. (2012). Changes in climate extremes and their impacts on the natural physical environment. *Managing the Risks of Extreme Events and Disasters to Advance Climate Change Adaptation: Special Report of the Intergovernmental Panel on Climate Change*, *9781107025*, 109–230. https://doi.org/10.1017/CBO9781139177245.006

[54] Sillmann, J., Thorarinsdottir, T., Keenlyside, N., Schaller, N., Alexander, L. V., Hegerl, G., Seneviratne, S. I., Vautard, R., Zhang, X., & Zwiers, F. W. (2017). Understanding, modeling and predicting weather and climate extremes: Challenges and opportunities. *Weather and Climate Extremes*, *18*(October), 65–74. https://doi.org/10.1016/j.wace.2017.10.003

[55] Sperling, F., & Szekely, F. (2005). *Disaster risk management in a changing climate*. Vulnerability and Adaptation Resource Group (VARG).

[56] Teshome, A., & Zhang, J. (2019). Increase of extreme drought over Ethiopia under climate warming. *Advances in Meteorology*, *2019*. https://doi.org/10.1155/2019/5235429

[57] Trenberth, K. E. (2021). *ENSO in the Global Climate System*. 21–37.

[58] Wang, F., Zhang, C., & Zhou, H. (2014). *Diurnal temperature range variation and its causes in a semiarid region from 1957 to 2006*. *December 2017*. https://doi.org/10.1002/joc.3690

[59] Wang, Q., Wang, M., Fan, X., Zhang, F., & Zhu, S. (2017). *Trends of temperature and precipitation extremes in the Loess Plateau Region of China, 1961 – 2010*. 949–963. https://doi.org/10.1007/s00704-016-1820-z

[60] Welzer, H. (2012). Darfur: The First Climate War. *Audubon Society*.

[61] Worku, M. A. (2021). *Variability and time series trend analysis of temperature over 1981-2018 in semi-arid Borana zone, southern Ethiopia*. 0–27.

[62] Worku, M. A., Feyisa, G. L., & Beketie, K. T. (2022). Climate trend analysis for a semi-arid Borana zone in southern Ethiopia during 1981–2018. *Environmental Systems Research*, *11*(1). https://doi.org/10.1186/s40068-022-00247-7

[63] Yue, S., Pilon, P., & Cavadias, G. (2002). Power of the Mann–Kendall and Spearman's rho tests for detecting monotonic trends in hydrological series. *Journal of hydrology*, *259*(1–4), 254–271.